

# Bayesian filtering in incoherent scatter plasma parameter fits

Ilkka I. Virtanen<sup>1</sup>, Habtamu W. Tesfaw<sup>1</sup>, Lassi Roininen<sup>2</sup>, Sari Lasanen<sup>3</sup>, and  
Anita Aikio<sup>1</sup>

<sup>1</sup>Space Physics and Astronomy Research Unit, University of Oulu, Oulu, Finland

<sup>2</sup>School of Engineering Science, Lappeenranta-Lahti University of Technology, Lappeenranta, Finland

<sup>3</sup>Sodankylä Geophysical Observatory, University of Oulu, Sodankylä, Finland

## Key Points:

- Full-profile incoherent scatter analysis is implemented by means of Bayesian filtering and correlation priors.
- The technique reaches high time resolutions and enables ion composition fits.
- We have implemented the technique as an additional module to the GUISDAP incoherent scatter analysis tool.

---

Corresponding author: Ilkka I. Virtanen, [ilkka.i.virtanen@oulu.fi](mailto:ilkka.i.virtanen@oulu.fi)

**Abstract**

Incoherent scatter (IS) radars are invaluable instruments for ionospheric physics, since they observe altitude profiles of electron density ( $N_e$ ), electron temperature ( $T_e$ ), ion temperature ( $T_i$ ) and line-of-sight plasma velocity ( $V_i$ ) from ground. However, the temperatures can be fitted to the observed IS spectra only when the ion composition is known, and resolutions of the fitted plasma parameters are often insufficient for auroral electron precipitation, which requires high resolutions in both range and time. The problem of unknown ion composition has been addressed by means of the full-profile analysis, which assumes that the plasma parameter profiles are smooth in altitude, or follow some pre-defined shape. In a similar manner, one could assume smooth time variations, but this option has not been used in IS analysis. We propose a plasma parameter fit technique based on Bayesian filtering, which we have implemented as an additional Bayesian Filtering Module (BAFIM) in the GUIDAP analysis package. BAFIM allows us to control gradients in both time and range directions for each plasma parameter separately. With BAFIM we can fit F<sub>1</sub> region ion composition together with  $N_e$ ,  $T_e$ ,  $T_i$  and  $V_i$ , and we have reached 4 s/900 m time/range steps in four-parameter fits of  $N_e$ ,  $T_e$ ,  $T_i$  and  $V_i$  in E region observations of auroral electron precipitation.

**1 Introduction**

Incoherent scatter (IS) radars are high-power, large-aperture radars that detect radio wave scattering from thermal fluctuations in the ionospheric plasma. Power spectral density of the scattered signal is a function of number density, temperature, bulk velocity, and ion-neutral collision frequency of a number of ion species and electrons (for example Swartz & Farley, 1979, and references therein). All these parameters cannot be fitted to the spectrum, and a commonly used approximation is the four-parameter fit of  $N_e$ ,  $T_e$ ,  $T_i$  and  $V_i$ . Equal temperatures and bulk velocities are assumed for all ion species, and the ion-neutral collision frequency and ion composition are taken from ionospheric models.

In the F<sub>1</sub> region the four-parameter fit often produces incorrect temperatures (for example Blelly & van Eyken, 2010), because ion composition models are unreliable in the transition region from the E region molecular NO<sup>+</sup> and O<sub>2</sub><sup>+</sup> ions to the F<sub>2</sub> region atomic O<sup>+</sup>. Incorrect compositions bias the temperatures, because the IS spectrum is sensitive to the ratio  $T_i/m_i$ , where  $m_i$  is the mean ion mass. This is known as the "temperature-ion composition ambiguity" (TICA) (Martínez-Ledesma et al., 2019). Several authors have addressed the TICA problem by means of modeling the F<sub>1</sub> region temperature and ion composition profiles (Kelly & Wickwar, 1981; Cabrit & Kofman, 1996; Blelly & van Eyken, 2010; Zettergren et al., 2011; Häggström & Collis, 1990). Also direct estimation of both ion composition and temperature has been reported by Lathuillere, Lejeune, and Kofman (1983), but coarse resolutions were used, since such fits require extremely accurate IS spectra (Martínez-Ledesma et al., 2019).

Even the four-parameter fits are extremely challenging with a few second and a few hundred meter resolutions that are needed in observations of auroral electron precipitation. In high-resolution observations one may replace the fitted  $N_e$  with the raw electron density (scaled back-scattered power)  $N_r$ . For example Semeter and Kamalabadi (2005), Dahlgren et al. (2011), and Virtanen et al. (2018) used  $N_r$  in estimation of primary energy spectra of precipitating electrons. However,  $N_r$  equals  $N_e$  only if  $T_e = T_i$ , which may be an unjustified assumption when the precipitation heats the electron gas.

We propose an IS analysis technique that combines Bayesian filtering (for example Särkkä, 2013) in time and correlation priors (Roininen et al., 2011) in range. The combination allows us to extend the idea of full-profile IS analysis (Holt et al., 1992; Lehtinen et al., 1996a; Hysell et al., 2008), which assumes smoothness in range, to an assumption of smoothness in both time and range. With this approach we can fit ion compo-

sitions if both ion temperature and composition are assumed to vary smoothly with time and altitude, and we can include temperature fits in high-resolution electron density fits.

In Section 2 we give introduction to IS plasma parameter fits, Bayesian filtering and correlation priors. In Section 3 we explain how the prior models and Bayesian filtering are used in IS analysis and implemented as a 'Bayesian Filtering Module' (BAFIM) in GUIDAP. In Section 4 we demonstrate BAFIM fits of  $N_e$ ,  $T_e$ ,  $T_i$ ,  $V_i$ , and ion composition  $p=[O^+]/N_e$  in the F<sub>1</sub> region, and high-resolution fits of  $N_e$ ,  $T_e$ ,  $T_i$ , and  $V_i$  in the E region.

## 2 Theoretical background

Incoherent scatter signal from a small plasma volume is a zero-mean random process with autocorrelation function  $R(\tau)$ , where  $\tau$  is time lag. IS radar data are discrete samples of the autocorrelation function at discrete ranges  $r_i$ , times  $t_j$ , and lags  $\tau_k$ . Power spectral density of the scattered signal, which is the Fourier transform of the autocorrelation function, is a known function of plasma parameters (for example Swartz & Farley, 1979, and references therein).

Typically, plasma parameters are extracted from the autocorrelation function samples by non-linear least-squares methods with optimization techniques such as Levenberg-Marquardt algorithm. Alternatively, Markov chain Monte Carlo methods can be used for parameter extraction (for example Virtanen et al., 2014), although optimization has remained as academic standard in IS analysis.

### 2.1 Gated analysis and full profile analysis

IS analysis techniques can be roughly divided into 'gated' and 'full-profile' techniques. In gated analysis one runs the fitting process for each range  $r_i$  and time  $t_j$  independently from the analysis of neighbouring observational volumes. The EISCAT IS analysis tool GUIDAP (Lehtinen & Huuskonen, 1996) makes gated analysis. In full-profile analysis one fits range profiles of plasma parameters. Main benefit of the full-profile analysis is the possibility to include prior information of plasma parameter altitude profiles.

In its most general form the full-profile analysis performs also deconvolution of lag profiles (Holt et al., 1992; Hysell et al., 2008). A simpler approach is to use phase-coding, for example alternating codes (Lehtinen & Haggström, 1987), and to decode the autocorrelation function samples into high resolution before the plasma parameter fit (Lehtinen et al., 1996b). The two-stepped approach can be accomplished with arbitrary transmission modulations if the deconvolution is performed by statistical inversion (Virtanen et al., 2008, 2009). It is technically possible to add prior information already in the lag profile inversion step, but expressing the prior in terms of the actual plasma parameters is difficult in this approach.

### 2.2 Bayesian filtering and smoothing

Bayesian filtering (for example Särkkä, 2013) is a class of methods for estimating the state of a system from noisy indirect measurements. In IS analysis the state of the system reduces to point estimates of plasma parameter values and their standard deviations, while the indirect measurements are the observed autocorrelation function samples  $\mathbf{R}$ .

The filtering consists of a sequence of *prediction* and *update* steps. The sequence starts from an initial set of parameters  $\mathbf{x}_1^-$  and its covariance matrix  $\mathbf{P}_1^-$ , which form our prior understanding of the unknown parameters at time  $t_1$ . Autocorrelation function sam-

ples  $\mathbf{R}_1$  are then used to update the prior model into our best estimates of the parameters and their covariance at time  $t_1$ ,  $\mathbf{x}_1$  and  $\mathbf{P}_1$ . The update step is accomplished using a *measurement model*  $M$ ,

$$\mathbf{x}_1 = M(\mathbf{x}_1^-, \mathbf{P}_1^-, \mathbf{R}_1). \quad (1)$$

The update step is followed by a prediction step, in which  $\mathbf{x}_1$  and  $\mathbf{P}_1$  are combined with our best understanding of dynamics of the system to create our best prediction of the parameters and their covariance at time  $t_2$ ,  $\mathbf{x}_2^-$  and  $\mathbf{P}_2^-$ . The prediction step is accomplished using a *dynamic model*  $D$ ,

$$\mathbf{x}_2^- = D(\mathbf{x}_1, \mathbf{P}_1). \quad (2)$$

108 Measurements from time  $t_2$  are then used to update the prediction into the final esti-  
109 mates  $\mathbf{x}_2$  and  $\mathbf{P}_2$ , etc.

The simplest 'dynamic' model is to assume that the parameter values at subsequent time steps are close to each other, which reduces the prediction step into

$$\mathbf{x}_j^- = \mathbf{x}_{j-1}, \quad (3)$$

$$\mathbf{P}_j^- = \mathbf{P}_{j-1} + \mathbf{Q}, \quad (4)$$

110 where  $\mathbf{Q}$  is the *system noise covariance matrix*. The larger values  $\mathbf{Q}$  has in its diagonal,  
111 the smaller is the correlation between subsequent state estimates and the larger is the  
112 *filter gain*.

113 Bayesian filtering allows one to recursively estimate unknowns using the whole time  
114 history of measurements. In Bayesian smoothing the idea is extended to use of also 'fu-  
115 ture' measurements. Bayesian smoothing reduces variances of the unknown parameters  
116 and guarantees that equal amount of information from 'past' and 'future' measurements  
117 is included in each estimate of the unknowns. This removes a time shift that may be pro-  
118 duced by a low-gain filter.

If the dynamic and measurement models are linear functions, Bayesian smoothing can be implemented as a recursive smoothing step called *Rauch-Tung-Striebel* (RTS) smoother (Rauch, 1963). The smoothing recursion runs backwards in time using equations

$$\mathbf{G}_j = \mathbf{P}_j \mathbf{D}_j^T (\mathbf{P}_{j+1}^-)^{-1}, \quad (5)$$

$$\mathbf{x}_j^s = \mathbf{x}_j + \mathbf{G}_j (\mathbf{x}_{j+1}^s - \mathbf{x}_{j+1}^-), \quad (6)$$

$$\mathbf{P}_j^s = \mathbf{P}_j + \mathbf{G}_j (\mathbf{P}_{j+1}^s - \mathbf{P}_{j+1}^-) \mathbf{G}_j^T, \quad (7)$$

119 where  $\mathbf{D}_j$  is the theory matrix of the linear dynamic model  $D$  and the superscript  $T$  de-  
120 notes matrix transpose.  $\mathbf{x}_j^s$  and  $\mathbf{P}_j^s$  form the Bayesian smoothing solution of the prob-  
121 lem.

### 122 2.3 Correlation priors

Correlation priors (Roininen et al., 2011) allow one to model mutual covariances of the unknowns of an inverse problem in a well controlled way. Assuming that our prior belief of the unknowns  $\mathbf{x}$  is  $\mathbf{x}_p$ , the prior can be expressed as a linear inverse problem

$$\mathbf{m}_p = \begin{pmatrix} \mathbf{x}_p \\ \mathbf{0} \\ \mathbf{0} \end{pmatrix} = \mathbf{A}_p \mathbf{x} + \boldsymbol{\varepsilon}_p = \begin{pmatrix} \mathbf{A}_{p,0} \\ \mathbf{A}_{p,1} \\ \mathbf{A}_{p,2} \end{pmatrix} \mathbf{x} + \begin{pmatrix} \boldsymbol{\varepsilon}_{p,0} \\ \boldsymbol{\varepsilon}_{p,1} \\ \boldsymbol{\varepsilon}_{p,2} \end{pmatrix}, \quad (8)$$

where  $\mathbf{x}_p$  are prior values of the unknown parameters and  $\boldsymbol{\varepsilon}_p$  are discrete white noise with variances given in (18), (19), and (20). The theory matrix  $\mathbf{A}_p$  is constructed from ze-

roth, first and second order differences  $\mathbf{A}_{p,0}$ ,  $\mathbf{A}_{p,1}$ , and  $\mathbf{A}_{p,2}$ , as explained below. Covariance and mean of the prior can be solved from (8) as

$$\boldsymbol{\Sigma}'_p = (\boldsymbol{\Omega}_p)^{-1} = (\mathbf{A}_p^T \boldsymbol{\Sigma}_p^{-1} \mathbf{A}_p)^{-1}, \quad (9)$$

$$\mathbf{x}'_p = \boldsymbol{\Sigma}'_p \mathbf{A}_p^T \boldsymbol{\Omega}_p \mathbf{m}_p, \quad (10)$$

123 where  $\boldsymbol{\Sigma}_p$  is the error covariance of  $\boldsymbol{\varepsilon}_p$ ,  $\boldsymbol{\Omega}_p$  is the precision matrix,  $\mathbf{x}'_p$  is the final prior  
 124 mean, and  $\boldsymbol{\Sigma}'_p$  is its error covariance matrix. It is important to notice that the initial pro-  
 125 file is smoothed by the correlations and  $\mathbf{x}'_p \neq \mathbf{x}_p$ . In high-dimensional problems it is  
 126 important that  $\boldsymbol{\Omega}_p$  is a sparse matrix (Norberg et al., 2018).

The zeroth order part of the prior is

$$\mathbf{A}_{p,0} = \mathbf{I}, \quad (11)$$

$$\boldsymbol{\Sigma}_{p,0} = \text{diag}(\sigma_{p,0,1}^2, \sigma_{p,0,2}^2, \dots, \sigma_{p,0,N}^2), \quad (12)$$

where the diagonal error covariance matrix  $\boldsymbol{\Sigma}_{p,0}$  contains the prior variances of  $\mathbf{x}_p$ . The first order terms are

$$\mathbf{A}_{p,1} = \begin{pmatrix} 1 & -1 & 0 & \dots & 0 & 0 \\ 0 & 1 & -1 & \dots & 0 & 0 \\ 0 & 0 & 1 & \dots & 0 & 0 \\ \vdots & \vdots & \vdots & \ddots & \vdots & \vdots \\ 0 & 0 & 0 & \dots & 1 & -1 \end{pmatrix}, \quad (13)$$

$$\boldsymbol{\Sigma}_{p,1} = \text{diag}(\sigma_{p,1,1}^2, \sigma_{p,1,2}^2, \dots, \sigma_{p,1,N-1}^2), \quad (14)$$

and the second order terms are

$$\mathbf{A}_{p,2} = \begin{pmatrix} 1 & -2 & 1 & 0 & \dots & 0 & 0 & 0 \\ 0 & 1 & -2 & 1 & \dots & 0 & 0 & 0 \\ 0 & 0 & 1 & -2 & \dots & 0 & 0 & 0 \\ \vdots & \vdots & \vdots & \vdots & \ddots & \vdots & \vdots & \vdots \\ 0 & 0 & 0 & 0 & \dots & 1 & -2 & 1 \end{pmatrix}, \quad (15)$$

$$\boldsymbol{\Sigma}_{p,2} = \text{diag}(\sigma_{p,2,1}^2, \sigma_{p,2,2}^2, \dots, \sigma_{p,2,N-2}^2). \quad (16)$$

The full prior covariance matrix  $\boldsymbol{\Sigma}_p$  is

$$\boldsymbol{\Sigma}_p = \begin{pmatrix} \boldsymbol{\Sigma}_{p,0} & \mathbf{0} & \mathbf{0} \\ \mathbf{0} & \boldsymbol{\Sigma}_{p,1} & \mathbf{0} \\ \mathbf{0} & \mathbf{0} & \boldsymbol{\Sigma}_{p,2} \end{pmatrix}. \quad (17)$$

Variances of the zeroth, first and second order terms are (Roininen et al., 2011),

$$\sigma_{p,0,i}^2 = c_0^{-1} \alpha_i \ell_i / \Delta h_i, \quad (18)$$

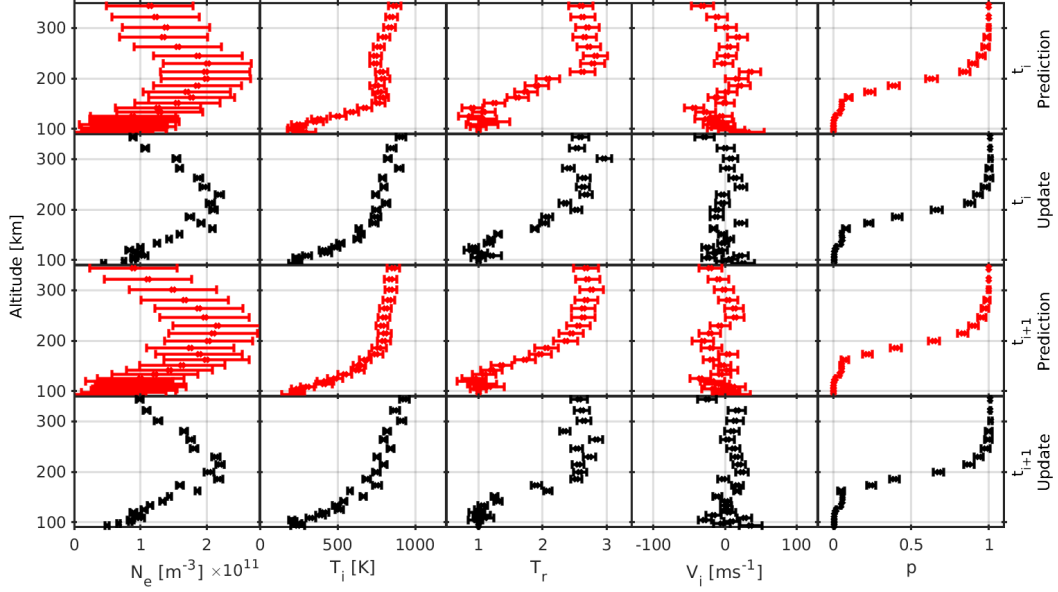
$$\sigma_{p,1,i}^2 = c_1^{-1} \alpha_i \Delta h_i / \ell_i = c_0 / c_1 \sigma_{p,0,i}^2 (\Delta h_i / \ell_i)^2, \quad (19)$$

$$\sigma_{p,2,i}^2 = c_2^{-1} \alpha_i (\Delta h_i / \ell_i)^3 = c_0 / c_2 \sigma_{p,0,i}^2 (\Delta h_i / \ell_i)^4, \quad (20)$$

127 where  $\alpha_i$  is *correlation power* in the  $i^{\text{(th)}}$  range gate,  $\Delta h_i$  is width of the  $i^{\text{(th)}}$  range gate,  
 128 and  $\ell_i$  is the corresponding *correlation length*. The correlation lengths define how smooth  
 129 the profile is, and the correlation power defines width of the prior distribution. The con-  
 130 stants  $c_0$ ,  $c_1$ ,  $c_2$  define shape of the final covariance structure. For example,  $c_0 = 1$ ,  $c_1 =$   
 131  $1/2$ ,  $c_2 = 1/8$  produces a Gaussian covariance. The model variances depend on the dis-  
 132 cretization and correlation length in a way that makes the model essentially grid-independent.

### 3 BAFIM implementation

We have implemented an IS analysis tool based on Bayesian filtering in time and correlation priors in range as an additional *Bayesian filtering module* (BAFIM) to the



134 **Figure 1.** Prediction and update steps of BAFIM. Predicted altitude profiles of  $N_e$ ,  $T_i$ ,  $T_r$ ,  $V_i$ ,  
 135 and  $p$  at time  $t_i$  (first row), updated profiles at  $t_i$  (second row), predicted profiles at  $t_{i+1}$  (third  
 136 row), and updated profiles at  $t_{i+1}$ .

GUIDSAP IS analysis tool (Lehtinen & Huuskonen, 1996). We assume a five parameter fit of electron number density  $N$ , ion temperature  $T$ , ion-to-electron temperature ratio  $E$ , line-of-sight plasma velocity  $V$  and ion composition  $O = [O^+]/N$ , where  $O^+$  is the  $O^+$  ion number density. We use the alternative notation ( $N=N_e$ ,  $T=T_i$ ,  $E=T_r$ ,  $V=V_i$ ,  $O=p$ ) in this section to simplify the equations. The vector of plasma parameters at time step  $j$  is

$$\mathbf{x}_j = (\mathbf{N}_j, \mathbf{T}_j, \mathbf{E}_j, \mathbf{V}_j, \mathbf{O}_j)^T, \quad (21)$$

where  $\mathbf{N}_j$  is the electron density profile in range gates  $i = 1, \dots, M$ ,

$$\mathbf{N}_j = (N_{1,j}, N_{2,j}, \dots, N_{M,j}), \quad (22)$$

137 and the vectors of the other parameters are defined similarly.

138 The analysis starts from an initial guess of the plasma parameters at time  $t_1$ ,  $\mathbf{x}_1^-$ ,  
 139 and their covariance  $\mathbf{P}_1^-$ . The parameters  $\mathbf{x}_1^-$  are from the International Reference Ionosphere (IRI) model (Bilitza et al., 2017), and  $\mathbf{P}_1^-$  is a diagonal matrix with variances equal  
 140 to the *process noise variances*, defined in (35), in its diagonal. The parameters  $\mathbf{x}_1^-$  and  
 141 their variances  $\sigma_1^{2-} = \text{diag}(\mathbf{P}_1^-)$  are used as a prior in a normal GUIDSAP fit to mea-  
 142 surements  $\mathbf{R}_1$ . The GUIDSAP fit is the update step of the Bayesian filter. The gated  
 143 GUIDSAP analysis does not produce a full error covariance matrix of  $\mathbf{x}_1$ , but the error  
 144 covariance matrix  $\mathbf{P}_1$  contains mutual correlations of plasma parameters in each range  
 145 gate.  
 146

147 After the first time step, priors for the following GUIDSAP fits are not taken from  
 148 the IRI model, but the fit results from  $t_1$  are used to predict the parameters and their  
 149 covariance at  $t_2$ . The predicted values  $\mathbf{x}_2^-$  and  $\mathbf{P}_2^-$  are used as a prior to fit  $\mathbf{x}_2$  and  $\mathbf{P}_2$   
 150 to measurements  $\mathbf{R}_2$ ,  $\mathbf{x}_2$  and  $\mathbf{P}_2$  are used to calculate the predicted  $\mathbf{x}_3^-$  and  $\mathbf{P}_3^-$ , etc. The  
 151 analysis steps are illustrated in Figure 1, whose first row shows predicted altitude pro-  
 152 files of  $N=N_e$ ,  $T=T_i$ ,  $E=T_r$ ,  $V=V_i$ , and  $O=p$  at time  $t_i$ . The predictions are used as pri-  
 153 ors in a GUIDSAP fit, which produces the updated profiles on the second row. The pro-  
 154 files on the second row are used to predict the parameter profiles at time  $t_{i+1}$  (third row),

155 the prediction is used as a prior when fitting the parameters at time  $t_{i+1}$  (fourth row),  
 156 etc.

In the prediction step, a correlation prior is used to create smooth plasma parameter profiles. The measurements  $\mathbf{x}_1$  and their covariance  $\mathbf{P}_1$  are used as the zeroth order terms in (8),

$$\mathbf{x}_p = \mathbf{x}_1, \quad (23)$$

$$\boldsymbol{\Sigma}_{p,0} = \mathbf{P}_1. \quad (24)$$

The first and second order differences in (8) are then formed for each plasma parameter separately. Variances of the plasma parameters  $\mathbf{x}_1 = (\mathbf{N}_1, \mathbf{T}_1, \mathbf{E}_1, \mathbf{V}_1, \mathbf{O}_1)^T$  are

$$\boldsymbol{\sigma}_{p,0}^2 = (\boldsymbol{\sigma}_{N,0}^2, \boldsymbol{\sigma}_{T,0}^2, \boldsymbol{\sigma}_{E,0}^2, \boldsymbol{\sigma}_{V,0}^2, \boldsymbol{\sigma}_{O,0}^2)^T = \text{diag}(\mathbf{P}_1). \quad (25)$$

The first order difference matrices (13) for each parameter are identical  $M \times M - 1$  matrices,  $\mathbf{A}_{N,1} = \mathbf{A}_{T,1} = \mathbf{A}_{E,1} = \mathbf{A}_{V,1} = \mathbf{A}_{O,1}$ , and the full first order difference matrix is the block diagonal matrix

$$\mathbf{A}_{p,1} = \begin{pmatrix} \mathbf{A}_{N,1} & \mathbf{0} & \mathbf{0} & \mathbf{0} & \mathbf{0} \\ \mathbf{0} & \mathbf{A}_{T,1} & \mathbf{0} & \mathbf{0} & \mathbf{0} \\ \mathbf{0} & \mathbf{0} & \mathbf{A}_{E,1} & \mathbf{0} & \mathbf{0} \\ \mathbf{0} & \mathbf{0} & \mathbf{0} & \mathbf{A}_{V,1} & \mathbf{0} \\ \mathbf{0} & \mathbf{0} & \mathbf{0} & \mathbf{0} & \mathbf{A}_{O,1} \end{pmatrix}. \quad (26)$$

Variances of the first order terms are calculated from (19). First order variances for electron density are

$$\sigma_{N,1,i}^2 = c_0/c_1 \sigma_{N,0,i}^2 (\Delta h_i / \ell_{N,i})^2, \quad (27)$$

and variances of the other parameters are calculated in a similar manner. The first order covariance matrix is the diagonal matrix

$$\boldsymbol{\Sigma}_{p,1} = \text{diag}(\boldsymbol{\sigma}_{N,1}^2, \boldsymbol{\sigma}_{T,1}^2, \boldsymbol{\sigma}_{E,1}^2, \boldsymbol{\sigma}_{V,1}^2, \boldsymbol{\sigma}_{O,1}^2). \quad (28)$$

157 The second order differences and their variances are formed in a similar manner. As a  
 158 result, we have a matrix equation of the form (8), from which parameter profiles smoothed  
 159 in range,  $\mathbf{x}'$ , and their covariance,  $\boldsymbol{\Sigma}'$ , can be solved using (9) and (10).

The smoothed parameter profiles  $\mathbf{x}'$  are used as the prediction for time step  $t_2$ ,

$$\mathbf{x}_2^- = \mathbf{x}', \quad (29)$$

and the predicted covariance is the sum of the covariance of  $\mathbf{x}'$  and a process noise covariance  $\mathbf{Q}$ ,

$$\mathbf{P}_2^- = \boldsymbol{\Sigma}' + \mathbf{Q}. \quad (30)$$

The process noise covariance is a diagonal  $5M \times 5M$  matrix with a different variance for each plasma parameter (35) in its diagonal,

$$\mathbf{Q} = \text{diag}(q_N, \dots, q_N, q_T, \dots, q_T, q_E, \dots, q_E, q_V, \dots, q_V, q_O, \dots, q_O). \quad (31)$$

The RTS smoother is implemented in BAFIM as a post-processing step. Since only the first  $5M$  elements of the vector  $\mathbf{m}_p$  are nonzero in (8) and (10), the matrix  $\mathbf{D}$  in (5) consists of the first  $5M$  columns of the  $5M \times (15M - 3)$  matrix

$$\mathbf{D}' = \boldsymbol{\Sigma}_s \mathbf{A}_p^T \boldsymbol{\Omega}_p. \quad (32)$$

160 The RTS smoother is only a linear approximation, but the approximation is reasonable  
 161 if the time steps are short enough to keep changes in plasma parameters small in between  
 162 subsequent time steps.

The correlation lengths  $\ell_i$  are proportional to the plasma scale height

$$H_i = \frac{k_B T_i (1 + E_i) / 2}{m_i g_i}, \quad (33)$$

calculated from the IRI model parameters. Here  $k_B$  is the Boltzmann constant,  $m_i$  is the mean ion mass,  $g_i$  is the acceleration of gravity, and the subscript  $i$  refers to the  $i^{\text{th}}$  range gate. The correlation lengths of  $N$  are

$$\ell_{N,i} = s_N^h H_i, \quad (34)$$

163 where  $s_N^h$  is a constant, and the correlation lengths of the other parameters are defined  
164 in a similar manner.

165 In the correlation prior, covariance of the zeroth order terms is the posterior co-  
166 variance  $\Sigma_{p,0} = \mathbf{P}_1$ , and variances of the first and second order terms are proportional  
167 to  $\ell_i^{-2}$  and  $\ell_i^{-4}$ , respectively. Thus, at the limit of small correlation lengths  $\ell_i$ , the smoothed  
168 profile  $\mathbf{x}'$  approaches the fitted profile  $\mathbf{x}_1$ , and the covariance  $\Sigma'$  approaches  $\mathbf{P}_1$ . BAFIM  
169 can thus be run without the smoothing in range if the correlation lengths  $\ell_i$  are small,  
170 i.e. the constants  $s^h$  are small.

The process noise variances  $q_N, q_T, q_E, q_V, q_O$  are proportional to the time step du-  
ration,

$$q_N = (s_N^t)^2 \Delta t, \quad (35)$$

171 etc. Each parameter is fitted within an altitude interval  $[h_{min}, h_{max}]$ , below  $h_{min}$  and  
172 above  $h_{max}$  the parameter is fixed to the IRI model value with a small variance. The  
173 heights  $h_{min,N}, h_{max,N}, h_{min,T}, h_{max,T}, \dots$ , the constants  $s_N^h, s_T^h, s_E^h, s_V^h, s_O^h$ , and the  
174 constants  $s_N^t, s_T^t, s_E^t, s_V^t, s_O^t$  are user inputs and may vary from one analysis run to an-  
175 other.

## 176 4 Plasma parameter fits with BAFIM

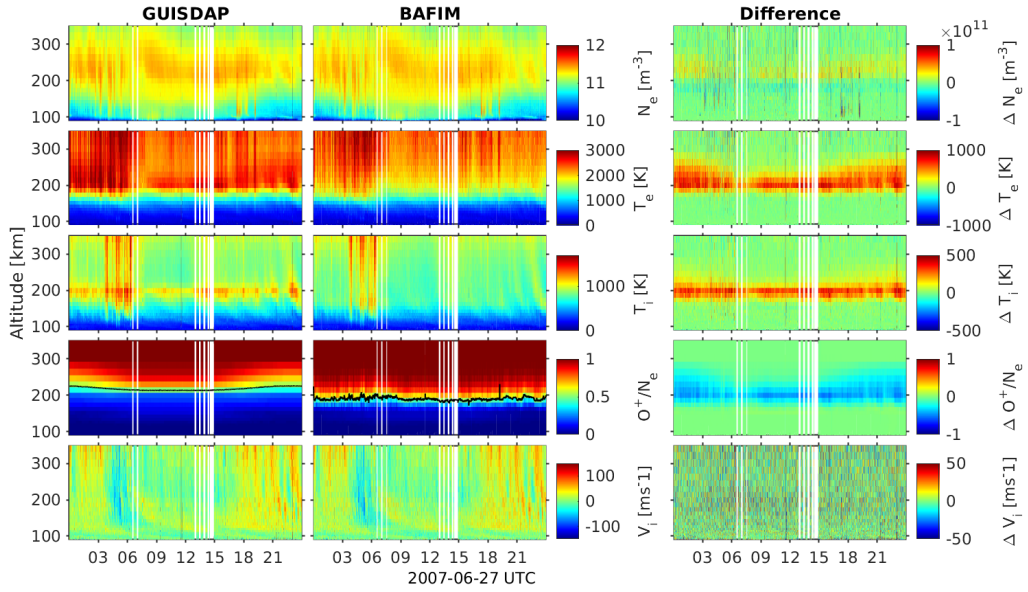
177 In this section we demonstrate plasma parameter fits with BAFIM in two use cases,  
178 ion composition fits in the F<sub>1</sub> region and high-resolution E region analysis during au-  
179 roral electron precipitation. We use field-aligned observations from the EISCAT Sval-  
180 bard radar (ESR) and the EISCAT UHF radar. We consider fits of electron density ( $N_e$ ),  
181 ion temperature ( $T_i$ ), ion-to-electron temperature ratio ( $T_r$ ), line-of-sight plasma bulk  
182 velocity ( $V_i$ ), and ion composition ( $p = [O^+]/N_e$ ). In the results we show the electron  
183 temperature  $T_e = T_i \cdot T_r$  instead of  $T_r$ . While the assumption of smoothness in range  
184 is necessary in the selected demonstrations, we emphasize that BAFIM can be used also  
185 without this assumption, for example to improve time resolution of four-parameter fits  
186 in low-elevation or bistatic observations. In this section, standard GUIDAP fits and GUID-  
187 DAP fits with BAFIM are referred to as 'GUIDAP' and 'BAFIM', correspondingly.

### 188 4.1 Ion composition fits

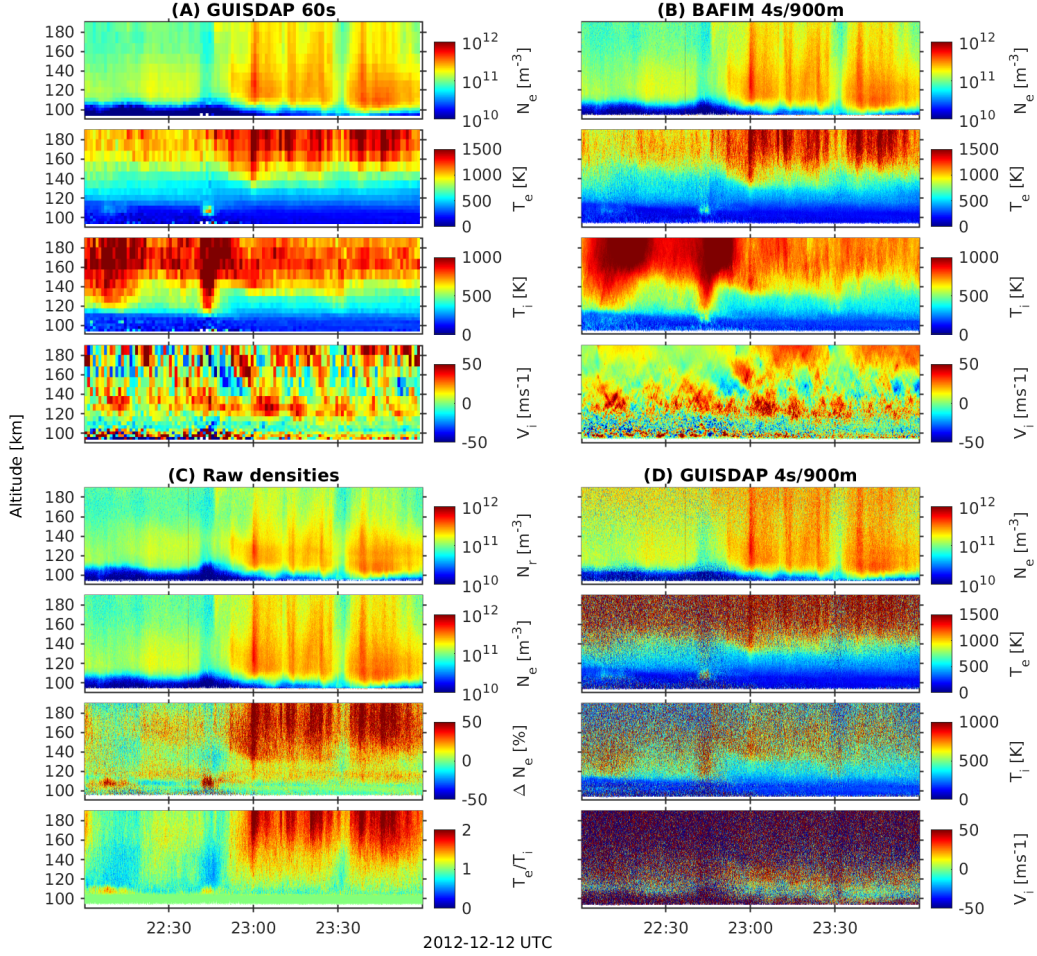
196 Ion frictional heating occurs when an electric field drives the ionospheric plasma  
197 through the neutral atmosphere and the ion gas is heated in collisions with neutral par-  
198 ticles. The heating may affect F<sub>1</sub> region ion composition, because reaction rates of some  
199 important charge-exchange reactions depend on temperature, and expansion of the neu-  
200 tral atmosphere may increase neutral N<sub>2</sub> concentration in the F region (Kelly & Wick-  
201 war, 1981). Deviations from the IRI ion composition may bias F<sub>1</sub> region ion tempera-  
202 ture estimates in four-parameter GUIDAP fits of  $N_e, T_e, T_i$  and  $V_i$ . An example of such  
203 an event is shown on the left in Figure 2, where four-parameter GUIDAP fit results with  
204 60 s resolution are shown for 24 hours of ESR data. Ion temperature (third panel on the  
205 left) has an artificial local maximum around 200 km altitude, where IRI predicts too much  
206 molecular ions (fourth panel).

189 **Table 1.** BAFIM settings used in the data analysis.  $N_e$ ,  $T_i$ ,  $T_r$ , and  $V_i$  are fitted at all altitudes  
 190 above  $h_{min}$ .  $p$  is not fitted at all in the E region analysis of the UHF data. The constants  $s^h$  and  
 191  $s^t$  are scaling factors that control smoothness of the solutions in range and time, respectively, as  
 192 explained in Section 3.

	ESR 27 June 2007				UHF 12 December 2012			
	$s^h$	$s^t$	$h_{min}$ (km)	$h_{max}$ (km)	$s^h$	$s^t$	$h_{min}$ (km)	$h_{max}$ (km)
$N_e$	0.1	$2.5 \cdot 10^{10} \text{ m}^{-3} \text{ s}^{-1/2}$	0	-	1.0	$2.5 \cdot 10^{11} \text{ m}^{-3} \text{ s}^{-1/2}$	0	-
$T_i$	0.3	$10 \text{ K s}^{-1/2}$	80	-	0.2	$30 \text{ K s}^{-1/2}$	80	-
$T_r$	0.3	$0.05 \text{ s}^{-1/2}$	103	-	0.4	$0.1 \text{ s}^{-1/2}$	103	-
$V_i$	0.2	$2.5 \text{ ms}^{-3/2}$	80	-	0.1	$5 \text{ ms}^{-3/2}$	80	-
$p$	0.2	$0.003 \text{ s}^{-1/2}$	150	320	-	-	0	0



193 **Figure 2.** Ion composition analysis. GUIDAP four-parameter fit with 60 s resolution (left),  
 194 five-parameter BAFIM fit with 6 s time steps (middle), and difference of these two (GUIDAP -  
 195 BAFIM) (right). In the default GUIDAP fit the ion composition is from the IRI model.



221 **Figure 3.** High-resolution E region analysis. (A) GUISDAP fit with 60 s time resolution and  
 222 range resolution varying from 3 km to 13 km, (B) BAFIM fit with 4 s/900 m steps, (C)  $N_r$ ,  
 223 BAFIM-fitted  $N_e$ , relative difference  $\Delta N_e = (N_e - N_r)/N_r$ , and BAFIM  $T_e/T_i$ , (D) GUISDAP fit  
 224 with 4 s/900 m resolutions.

207 In five-parameter BAFIM fit of the same data (Figure 2, middle panels), also the  
 208 ion composition  $p$  is fitted, and the analysis proceeds with 6 s time steps. Other BAFIM  
 209 settings are listed in Table 1. The artificial ion temperature maximum, which is visible  
 210 in the GUISDAP fit, is not produced in the BAFIM fit. The transition altitude, where  
 211 number density of molecular ions is equal to  $O^+$  density ( $p = 50\%$ , black lines in the  
 212 fourth panels), is generally lower than in the IRI model. Difference of the two fit results  
 213 (GUISDAP - BAFIM) is shown on the right in Figure 2, where one can see how the differ-  
 214 ence in  $p$  affects also  $T_i$ ,  $T_e$  and even  $N_e$  profiles. While the artefact around 200 km  
 215 altitude was removed by BAFIM, the true ion frictional heating events between 4 and  
 216 7 UT, as well as the weaker  $T_i$  enhancements after 15 UT, are reproduced by BAFIM,  
 217 demonstrating its ability to maintain true ion temperature maxima. We note that our  
 218 results are very similar with those of Blelly and van Eyken (2010), who used the same  
 219 data to demonstrate a full-profile analysis technique based on ion energy equations.

220

## 4.2 High-resolution observations of auroral electron precipitation

225

226

227

228

229

230

231

232

IS radars can detect impact ionization and electron heating caused by auroral electron precipitation. While existing high-latitude IS radars can typically reach a time resolution of some tens of seconds in the four-parameter fits of  $N_e$ ,  $T_i$ ,  $T_r$ , and  $V_i$ , optical observations show that the precipitation may change substantially in a few seconds and even below (for example Dahlgren et al., 2016). High-resolution E region observations often rely on raw electron densities (for example Semeter & Kamalabadi, 2005; Dahlgren et al., 2011; Virtanen et al., 2018), which are calculated assuming  $T_e = T_i$ . However, this assumption may not be justified, since the precipitation heats the electron gas.

233

234

235

236

237

238

239

240

241

242

Figure 3 shows plasma parameter fit results from three different analysis runs of an EISCAT UHF radar measurement on 12 December 2012: (A) a four-parameter GUIDAP fit with 60 s time resolution and range resolution varying from 3 km to 13 km, (B) a BAFIM fit with 4 s/900 m steps, and (D) a GUIDAP fit with 4 s/900 m resolution. The BAFIM settings, listed in Table 1, were chosen so that electron densities in adjacent range and time steps are practically uncorrelated, and noise levels of the other parameters are acceptable. While plasma parameters from the GUIDAP fit are extremely noisy with the 4 s/900 m resolution, the BAFIM fit produces temperatures and velocities that match well with the standard coarse-resolution fit (for example, compare  $T_i$  and  $V_i$  in panels (A), (B), and (D)).

243

244

245

246

247

248

Importance of the temperature fit is demonstrated in Figure 3 (C), which shows raw electron density  $N_r$ , BAFIM-fitted  $N_e$ , relative difference  $(N_e - N_r)/N_r$ , and the temperature ratio  $T_e/T_i$ . The raw densities are clear underestimates after 22:50 UT, when electron precipitation heats the electron gas and  $T_e > T_i$ . This effect was neglected for example in Virtanen et al. (2018), because the high-resolution four-parameter fits were practically impossible.

249

## 5 Discussion

250

251

252

BAFIM is the first implementation of Bayesian filtering to IS plasma parameter fits. In this section we discuss some important properties of BAFIM and potential future improvements.

253

### 5.1 Resolutions of BAFIM fit results

254

255

256

257

258

259

260

261

262

263

While the BAFIM analysis proceeds with short steps in range and time, each fit result may contain information from considerably longer intervals because the steps are correlated. One should thus make a clear difference between the effective resolutions – the intervals in range and time which make significant contributions to the fit result – and the step sizes. The effective resolutions are not constants, but they depend on the amount of information gained from each individual measurement. Effective resolutions of each parameter at each altitude may be tuned separately by adjusting the corresponding process noise variances and correlation lengths. Effective resolutions of  $N_e$  are typically kept very close to the step sizes, while coarser effective resolutions are accepted for the other parameters to reach an acceptable statistical accuracy.

264

### 5.2 Tuning and validating BAFIM

265

266

267

268

269

Tuning the process noise variances and correlation lengths of BAFIM may be non-trivial, since the correlations in time allow part of the prior information introduced with the correlation priors to be passed from one time step to another. Any change in process noise variance must thus be compensated with a corresponding change in correlation length to keep the effective smoothing in range unchanged. In addition, changing

270 the process noise and correlation length of one plasma parameter may affect the others  
 271 due to error correlations.

272 In this paper, BAFIM was tuned to produce results that match with the default  
 273 GUIDAP fits with 60 s resolution. The only physics-based part of the model are the  
 274 correlation lengths, which are proportional to the plasma scale heights. Alternative ways  
 275 to tune the filter would be to derive theoretical limits for gradients in space and time,  
 276 or to extract information on the correlation structures from existing measurements. Cor-  
 277 relation structures of mesospheric winds have been extracted from meteor radar obser-  
 278 vations by Vierinen et al. (2019), and a similar work for incoherent scatter radars could  
 279 be possible.

280 Validation of BAFIM results, the ion composition fits in particular, is a challeng-  
 281 ing task due to lack of measurements from other instruments. Observations of F<sub>1</sub> region  
 282 ion composition are mainly from rockets, and the rocket observation would need to be  
 283 from vicinity of the radar beam to enable reasonable comparisons. Alternatively, one could  
 284 analyse simulated radar data corresponding a realistic model ionosphere. Such simula-  
 285 tions would be possible for example with the simISR tool (Swoboda et al., 2017).

### 286 5.3 Ion composition fits

287 In the ion composition fits a small process noise variance  $q_O$  was used for the ion  
 288 composition and a relatively large variance  $q_T$  was used for the ion temperature, which  
 289 is equivalent with the assumption that ion temperature varies much more rapidly than  
 290 ion composition. Only slow variations in composition were allowed, because allowing rapid  
 291 variations in both ion composition and temperature may lead to unrealistic oscillations  
 292 due to the temperature-ion composition ambiguity. With the selected tuning BAFIM  
 293 can follow the relatively slow ion composition variations associated with the large scale  
 294 convection electric field, but rapid variations caused by small scale electric fields around  
 295 auroral arcs are challenging.

296 Time resolution of the composition fits could be improved if physics-based mod-  
 297 els were included in the prediction step. One could either model the temperature pro-  
 298 files or include a chemistry model that solves temperature-dependent compositions. The  
 299 temperature profiles could be modeled, for example, with the techniques of Zettergren  
 300 et al. (2011) and Blelly and van Eyken (2010), while chemistry modeling could be adopted  
 301 for example from Richards and Voglozin (2011). Also D region ion composition and tem-  
 302 peratures could be observed if a sufficient model, for example the Sodankylä Ion and Neu-  
 303 tral Chemistry (SIC) model (Turunen et al., 2016) was used.

### 304 5.4 EISCAT\_3D

305 EISCAT\_3D (McCrea et al., 2015) is the next-generation geospace radar system  
 306 currently being built in northern Norway, Sweden, and Finland. The radar will provide  
 307 an order-of-magnitude improvement in measurement speed, and it will be the first mul-  
 308 tistatic, multibeam incoherent scatter radar system. EISCAT\_3D will be able to conduct  
 309 volumetric observations, including 3D observations of plasma flows.

310 If BAFIM-like analysis was applied to field-aligned EISCAT\_3D measurements, the  
 311 order-of-magnitude improvement would mean sub-second time steps in four-parameter  
 312 fits, and resolutions sufficient for rapidly varying conditions in association with aurora  
 313 in ion composition fits. The volumetric observations would allow one to implement 3D  
 314 models of the ionosphere in the prediction step. An EISCAT\_3D analysis tool could be  
 315 designed for the volumetric observations and could make optimal use of the multistatic,  
 316 multibeam data, following the idea of Virtanen et al. (2014).

## 6 Conclusions

We have introduced an incoherent scatter analysis technique that allows us to control plasma parameter gradients in both time and space using Bayesian filtering and correlation priors. The technique is implemented as a Bayesian filtering module (BAFIM) in the GUIDAP analysis package. BAFIM allows us to fit  $F_1$  region ion compositions and transition altitudes, and to include ion and electron temperatures in high-resolution plasma parameter fits, in field-aligned incoherent scatter measurements. Improvements provided by the new analysis tool were demonstrated with EISCAT radar data, including fits of  $F_1$  region ion composition and high-resolution E region plasma parameter fits during short-lived auroral precipitation events. The technique could be extended to volumetric, multistatic observations of the EISCAT 3D radar and supplemented with ion chemistry models.

## Acknowledgments

This work is supported by the Academy of Finland, application numbers 285474, 326240, and 301542, and the Kvantum institute of the University of Oulu. EISCAT is an international association supported by research organisations in China (CRIRP), Finland (SA), Japan (NIPR and STEL), Norway (NFR), Sweden (VR), and the United Kingdom (NERC). The EISCAT data and the GUIDAP software are available for download from the EISCAT web page (<http://www.eiscat.se>). BAFIM is available at <https://doi.org/10.5281/zenodo.4033904>.

## References

- Bilitza, D., Altadill, D., Truhlik, V., Shubin, V., Galkin, I., Reinisch, B., & Huang, X. (2017). International Reference Ionosphere 2016: From ionospheric climate to real-time weather predictions. *Space Weather*, *15*(2), 418-429. doi: 10.1002/2016SW001593
- Blelly, P.-L., & van Eyken, A. P. (2010). A new analysis method for determining polar ionosphere and upper atmosphere characteristics from ESR data: Illustration with IPY period. *J. Geophys. Res.*, *115*, A09322. doi: 10.1029/2009JA014876
- Cabrit, B., & Kofman, W. (1996). Ionospheric composition measurement by EISCAT using a global fit procedure. *Ann. Geophys.*, *14*, 1496-1505. doi: 10.1007/s00585-996-1496-2
- Dahlgren, H., Gustavsson, B., Lanchester, B. S., Ivchenko, N., Brändström, U., Whiter, D. K., . . . Marklund, G. (2011). Energy and flux variations across thin auroral arcs. *Ann. Geophys.*, *29*, 1699-1712. doi: 10.5194/angeo-29-1699-2011
- Dahlgren, H., Lanchester, B. S., Ivchenko, N., & Whiter, D. K. (2016). Electrodynamics and energy characteristics of aurora at high resolution by optical methods. *J. Geophys. Res. Space Physics*, *121*, 5966-5974. doi: 10.1002/2016JA022446
- Häggröm, I., & Collis, P. N. (1990). Ion composition changes during F-region density depletions in the presence of electric fields at auroral latitudes. *J. Atmos. Terr. Phys.*, *52*(6-8), 519-529. doi: 10.1016/0021-9169(90)90050-W
- Holt, J. M., Rhoda, D. A., Tetenbaum, D., & van Eyken, A. P. (1992). Optimal analysis of incoherent scatter radar data. *Radio Sci.*, *27*(3), 435-447. doi: 10.1029/91RS02922
- Hysell, D. L., Rodrigues, F. S., Chau, J. L., & Huba, J. D. (2008). Full profile incoherent scatter analysis at Jicamarca. *Ann. Geophys.*, *26*, 59-75. doi: 10.5194/angeo-26-59-2008
- Kelly, J. D., & Wickwar, V. B. (1981). Radar measurements of high-latitude ion composition between 140 and 300 km altitude. *J. Geophys. Res.*, *86*(A9), 7617-7626. doi: 10.1029/JA086iA09p07617
- Lathuillere, C., Lejeune, G., & Kofman, W. (1983). Direct measurements of ion com-

- 368 position with EISCAT in high-latitude  $F_1$  region. *Radio Sci.*, *18*(6), 887-893.  
 369 doi: 10.1029/RS018i006p00887
- 370 Lehtinen, M. S., & Häggström, I. (1987). A new modulation principle for in-  
 371 coherent scatter measurements. *Radio Sci.*, *22*, 625-634. doi: 10.1029/  
 372 RS022i004p00625
- 373 Lehtinen, M. S., & Huuskonen, A. (1996). General incoherent scatter analysis and  
 374 GUIDAP. *J. Atmos. Terr. Phys.*, *58*, 435-452. doi: 10.1016/0021-9169(95)  
 375 00047-X
- 376 Lehtinen, M. S., Huuskonen, A., & Pirttilä, J. (1996a). First experiences of full-  
 377 profile analysis with GUIDAP. *Ann. Geophys.*, *14*, 1487-1495. doi: 10.1007/  
 378 s00585-996-1487-3
- 379 Lehtinen, M. S., Huuskonen, A., & Pirttilä, J. (1996b). First experiences of full-  
 380 profile analysis with GUIDAP. *Ann. Geophys.*, *14*, 1487-1495.
- 381 Martínez-Ledesma, M., Quezada, D., & Andrés, M. (2019). Determination of the  
 382 Signal Fluctuation Threshold of the Temperature-Ion Composition Ambiguity  
 383 Problem Using Monte Carlo Simulations. *J. Geophys. Res. Space Physics*,  
 384 *124*(4), 2897-2919. doi: 10.1029/2018JA026217
- 385 McCrea, I., Aikio, A., Alfonsi, L., Belova, E., Buchert, S., Clilverd, M., ... Vierinen,  
 386 J. (2015). The science case for the EISCAT\_3D radar. *Prog. Earth Planet. Sc.*,  
 387 *2*(1). doi: 10.1186/s40645-015-0051-8
- 388 Norberg, J., Vierinen, J., Roininen, L., Orispää, M., Kauristie, K., Rideout, W. C.,  
 389 ... Lehtinen, M. S. (2018). Gaussian Markov Random Field Priors in Iono-  
 390 spheric 3-D Multi-Instrument Tomography. *IEEE Trans. Geosci. Remote*  
 391 *Sens.*, 1-13. doi: 10.1109/TGRS.2018.2847026
- 392 Rauch, H. R. (1963). Solutions to the linear smoothing problem. *IEEE T. Automat.*  
 393 *Contr.*, *8*(4), 371-372.
- 394 Richards, P. G., & Voglozin, D. (2011). Reexamination of ionospheric photochem-  
 395 istry. *J. Geophys. Res. Space Physics*, *116*(A8). doi: 10.1029/2011JA016613
- 396 Roininen, L., Lehtinen, M. S., Lasanen, S., Orispää, M., & Markkanen, M. (2011).  
 397 Correlation Priors. *Inverse Problems and Imaging*, *5*(1), 167-184. doi: 10  
 398 .3934/ipi.2011.5.167
- 399 Särkkä. (2013). *Bayesian Filtering and Smoothing*. Cambridge University Press.
- 400 Semeter, J., & Kamalabadi, F. (2005). Determination of primary electron spec-  
 401 tra from incoherent scatter radar measurements of the auroral  $E$  region. *Radio*  
 402 *Sci.*, *40*, RS2006. doi: 10.1029/2004RS003042
- 403 Swartz, W. E., & Farley, D. T. (1979). A Theory of Incoherent Scattering of  
 404 Radio Waves by a Plasma 5. The Use of the Nyquist Theorem in General  
 405 Quasi-Equilibrium Situations. *J. Geophys. Res.*, *84*(A5), 1930-1932. doi:  
 406 10.1029/JA084iA05p01930
- 407 Swoboda, J., Semeter, J., Zettergren, M., & Erickson, P. J. (2017). Observability  
 408 of ionospheric space-time structure with ISR: A simulation study. *Radio Sci.*,  
 409 *52*(2), 215-234. doi: 10.1002/2016RS006182
- 410 Turunen, E., Kero, A., Verronen, P. T., Miyoshi, Y., Oyama, S.-I., & Saito, S.  
 411 (2016). Mesospheric ozone destruction by high-energy electron precipitation  
 412 associated with pulsating aurora. *J. Geophys. Res. Atmos.*, *121*, 11852-11861.  
 413 doi: 10.1002/2016JD025015
- 414 Vierinen, J., Chau, J. L., Charuvil, H., Urco, J. M., Clahsen, M., Avsarkisov, V.,  
 415 ... Volz, R. (2019). Observing mesospheric turbulence with specular meteor  
 416 radars: A novel method for estimating second-order statistics of wind velocity.  
 417 *Earth and Space Science*, *6*(7), 1171-1195. doi: 10.1029/2019EA000570
- 418 Virtanen, I. I., Gustavsson, B., Aikio, A. T., Kero, A., Asamura, K., & Ogawa, Y.  
 419 (2018). Electron Energy Spectrum and Auroral Power Estimation from In-  
 420 coherent Scatter Radar Measurements. *J. Geophys. Res. Space Physics*, *123*,  
 421 6865-6887. doi: 10.1029/2018JA025636
- 422 Virtanen, I. I., Lehtinen, M. S., Nygrén, T., Orispää, M., & Vierinen, J. (2008). Lag

- 423 profile inversion method for EISCAT data analysis. *Ann. Geophys.*, *26*, 571-  
424 581. doi: 10.5194/angeo-26-571-2008
- 425 Virtanen, I. I., McKay-Bukowski, D., Vierinen, J., Aikio, A. T., Fallows, R., &  
426 Roininen, L. (2014, December). Plasma parameter estimation from multistatic,  
427 multibeam incoherent scatter data. *J. Geophys. Res. Space Physics*, *119*(12),  
428 10528-10543. doi: 10.1002/2014JA020540
- 429 Virtanen, I. I., Vierinen, J., & Lehtinen, M. S. (2009, July). Phase-coded pulse aperi-  
430 odic transmitter coding. *Ann. Geophys.*, *27*, 2799-2811. doi: 10.5194/angeo-  
431 -27-2799-2009
- 432 Zettergren, M., Semeter, J., Heinselman, C., & Diaz, M. (2011). Incoherent scatter  
433 radar estimation of F region ionospheric composition during frictional heating  
434 events. *J. Geophys. Res.*, *116*, A01318. doi: 10.1029/2010JA016035